

Numerical Study of Bubble Train Flow in a Square Vertical Mini-Channel: Influence of Length of the Flow Unit Cell

Martin Wörner¹, Bradut E. Ghidersa², Ahmad F. Shahab³

1: Forschungszentrum Karlsruhe, Institut für Reaktorsicherheit, Karlsruhe, Germany, woerner@irs.fzk.de

2: Forschungszentrum Karlsruhe, Institut für Reaktorsicherheit, Karlsruhe, Germany, ghidersa@irs.fzk.de

3: Universität Karlsruhe, Karlsruhe, Germany, AF.Shahab@web.de

Abstract Bubble train flow is a two-phase flow pattern that frequently occurs in narrow channels. It is characterized by a regular sequence of bubbles of identical shape which move with the same velocity. The flow is, therefore, fully described by a flow unit cell, which consists of a bubble and the liquid slug separating it from the next bubble. In this paper we use the volume-of-fluid method to perform direct numerical simulations of co-current air-oil bubble train flow in a square vertical channel of 2 mm width. Results of five simulations for different length of the flow unit cell are presented. It is found that, for the same axial pressure drop per unit length, the bubble velocity and the mean liquid velocity increase with increase of the length of the flow unit cell. The bubble diameter also increases but becomes almost constant for larger values of the length of the flow unit cell. The correlation of the bubble diameter with the capillary number, Ca , shows that there is a regime where the bubble diameter increases with Ca and one regime where it decreases with Ca . The border between both regimes is determined by a ratio of bubble length to channel width of about 1.2. The latter finding is new as in experimental studies from literature so far only the second regime is observed.

1 Introduction

The prevailing trend to miniaturize conventional fluidic systems and devices for applications in chemical engineering has fostered recent interest in multiphase transport in small channels. Potential applications include miniaturized heat exchangers (Schubert et al., 2001), evaporators, condensers, distillation units, liquid-liquid and gas-liquid reactors, and multiphase extraction and separation units. For multiphase micro process engineering a large benefit stems from operating with gas and liquid layers of defined geometry with a defined interface, unlike most macroscopic disperse systems which typically have a size distribution of bubbles in the continuous liquid (Hessel et al., 2004). Related to this, a further potential benefit is the operation in many parallel channels, each having the same two-phase flow pattern. For practical applications, this should allow for a favorable numbering up approach instead of scaling up.

The design and optimization of miniaturized devices, therefore, require knowledge of the basic hydro-dynamical phenomena of the two-phase flow in a *single* channel. Although the development of the micro particle image velocimetry has made great progress (Meinhart et al., 1999), this method has been used so far only for single phase flow and can not be used to measure the three-dimensional local velocity field of *both* phases in the entire mini- or micro-channel.

An alternative measure to provide the desired information is the direct numerical simulation method (DNS). Recently, we performed direct numerical simulations of the air-oil bubble train flow in a vertical square capillary of 2 mm width (Ghidersa, 2003; Ghidersa et al., 2004). Here, bubble train flow refers to the flow of a regular train of bubbles, having identical shape and distance from each other and moving with the same velocity. Bubble train flow is, therefore, fully described by a flow unit cell (FUC). In the numerical simulation, therefore, one can consider one bubble only and use periodic boundary conditions in axial direction to account for the influence of the leading and trailing bubble. Our numerical simulations covered two values of the capillary number, which is the main physical parameter characterizing two-phase flows in small channels. A comparison of the

DNS results with experimental data of Thulasidas et al. (1995) showed good agreement for the bubble velocity and the relative velocity of the phases (Ghidersa et al., 2003). However, the maximum diameter of the bubble was underestimated by the DNS. This was attributed to the fact that in the DNS a cubic flow unit cell was considered while in the experiment the axial length of the flow unit cell, L_{fuc}^* , is much larger than the channel width, W^* (Note that throughout this paper the superscript * is used to distinguish a dimensional quantity from its non-dimensional counterpart). The aim of the present paper is, therefore, to perform a detailed numerical investigation on the influence of the length of the flow unit cell. For this purpose five simulations with values of L_{fuc}^*/W^* ranging from 1 to 2 are performed. In these simulations the void fraction is $\varepsilon = 33\%$ and the same axial pressure drop per unit length is specified as input parameter.

In the remainder of this paper we first give in Section 2 the governing equations and shortly describe the numerical method of our in-house computer code used to perform the simulations. In this section we also give the numerical and physical parameters of the simulations. In Section 3 we discuss in detail the simulation results where we focus on the dependence of the bubble diameter and bubble velocity on the length of the flow unit cell and the capillary number, respectively. The paper is closed by conclusions to be presented in Section 4.

2 Computational set up

2.1 Governing equations

The non-dimensional conservation equations for mass and momentum of two immiscible incompressible Newtonian fluids can be written in the form

$$\nabla \cdot \mathbf{v}_m = 0 \quad (1)$$

$$\begin{aligned} \frac{\partial(\rho_m \mathbf{v}_m)}{\partial t} + \nabla \cdot \rho_m \mathbf{v}_m \mathbf{v}_m &= -\nabla P + \frac{1}{Re_{\text{ref}}} \nabla \cdot \mu_m (\nabla \mathbf{v}_m + (\nabla \mathbf{v}_m)^T) - (1-f) \frac{Eo_{\text{ref}}}{We_{\text{ref}}} \mathbf{e}_g \\ &+ Eu_{\text{ref}} \mathbf{e}_p + \frac{a_i \kappa \mathbf{n}_i}{We_{\text{ref}}} \end{aligned} \quad (2)$$

where the center-of-mass velocity, the mixture density, and the mixture viscosity are defined by

$$\mathbf{v}_m \equiv \frac{1}{U_{\text{ref}}^*} \frac{f \rho_l^* \mathbf{v}_l^* + (1-f) \rho_g^* \mathbf{v}_g^*}{f \rho_l^* + (1-f) \rho_g^*}, \quad \rho_m \equiv \frac{f \rho_l^* + (1-f) \rho_g^*}{\rho_l^*}, \quad \mu_m \equiv \frac{f \mu_l^* + (1-f) \mu_g^*}{\mu_l^*} \quad (3)$$

Here, ρ_l^* and ρ_g^* are the liquid and gas density, μ_l^* and μ_g^* are the (constant) liquid and gas viscosity, f is the liquid volumetric fraction within a mesh cell, \mathbf{v}_l^* and \mathbf{v}_g^* are the gas and liquid velocity, and U_{ref}^* is a reference velocity.

To allow for the use of periodic boundary conditions in the numerical simulation, the mixture momentum equation (2) involves the “reduced pressure”

$$P \equiv \frac{1}{\rho_l^* U_{\text{ref}}^{*2}} \left(p^* - \rho_l^* \mathbf{g}^* \cdot \mathbf{x}^* + \frac{|\Delta p^*|}{L_{\text{ref}}^*} \mathbf{e}_p \cdot \mathbf{x}^* \right) \quad (4)$$

Here, p^* is the actual pressure, $\mathbf{g}^* = g^* \mathbf{e}_g$ is the gravity vector, \mathbf{x}^* is the co-ordinate vector, and $|\Delta p^*|$ is the constant axial pressure drop per reference length L_{ref}^* (In the sequel we will use L_{ref}^* to

normalize all length scales). Due to the above decomposition, in equation (2) the influence of gravity is accounted for by the buoyancy force which involves the unit vector in direction of gravity, \mathbf{e}_g . Similarly, the axial pressure drop results in a body force term that involves the unit vector in axial direction, \mathbf{e}_p .

The definitions of the reference Reynolds number, Re_{ref} , reference Eötvös number, Eo_{ref} , reference Weber number, We_{ref} , and reference Euler number, Eu_{ref} , appearing in the mixture momentum equation (2) are

$$Re_{\text{ref}} \equiv \frac{\rho_l^* L_{\text{ref}}^* U_{\text{ref}}^*}{\mu_l^*}, \quad Eo_{\text{ref}} \equiv \frac{(\rho_l^* - \rho_g^*) g^* L_{\text{ref}}^{*2}}{\sigma^*}, \quad We_{\text{ref}} \equiv \frac{\rho_l^* L_{\text{ref}}^* U_{\text{ref}}^{*2}}{\sigma^*}, \quad Eu_{\text{ref}} \equiv \frac{|\Delta p^*|}{\rho_l^* U_{\text{ref}}^{*2}}, \quad (5)$$

where σ^* is the coefficient of surface tension. The last term in the mixture momentum equation (2) represents the surface tension force. In this term $a_i = a_i^* L_{\text{ref}}^*$ is the non-dimensional volumetric interfacial area concentration in the mesh cell, $\kappa = \kappa^* L_{\text{ref}}^*$ is twice the non-dimensional mean curvature of the interface and \mathbf{n}_i is the unit normal vector to the interface pointing into the liquid.

The set of equations is completed by the transport equation for the liquid volumetric fraction

$$\frac{\partial f}{\partial t} + \nabla \cdot f \mathbf{v}_m = 0 \quad (6)$$

which expresses - in the absence of phase change - the mass conservation of the liquid phase. The derivation of the above set of equations is given in Wörner et al. (2001). Here, the equations are already in simplified form. Namely, it is assumed that within a mesh cell both phases move with the same velocity, i.e. the center-of-mass velocity \mathbf{v}_m . This assumption corresponds to a locally homogeneous model.

2.2 Numerical method

We now give a short outline of the numerical method used in our in-house computer code TURBIT-VOF. The code is based on the finite volume method, uses Cartesian co-ordinates, and employs a regular staggered grid. The general solution strategy is based on a projection method where a conjugated gradient method is used to solve the resulting pressure Poisson equation. For approximation of spatial derivates a second order central difference scheme is used. The integration in time is done by a third order explicit Runge-Kutta method. The transport equation (6) for the liquid volumetric fraction is solved by a volume of fluid method which involves two steps. First, for each mesh cell that instantaneously contains both phases, the interface orientation and location is reconstructed using the PLIC (Piecewise Linear Interface Reconstruction Algorithm) method EPIRA that locally approximates the interface by a plane. In a second step the fluxes of liquid across the faces of the mesh cell are computed. For details about the numerical method we refer to Sabisch et al. (2001) and Ghidersa (2003).

2.3 Geometry and grid parameters

We define our coordinate system by taking y^* as stream-wise vertical direction and x^* and z^* as wall-normal directions. Thus, the gravity vector points in negative y^* -direction and we have $-\mathbf{e}_g = \mathbf{e}_p = \mathbf{e}_y$. We consider a computational domain of size $W^* \times L_{\text{fuc}}^* \times W^*$. As we normalize all length scales by $L_{\text{ref}}^* = W^* = 2$ mm the non-dimensional size of the computational box is $1 \times L_{\text{fuc}} \times 1$. In this paper we perform five simulations with L_{fuc} ranging from 1 to 2, see Table 1. Thus, in all the five simulations the channel has the same cross sectional area while the axial length of the flow domain differs. In all simulations the computational grid is uniform and consists of cubic mesh cells

of size $h = 1/48$. The use of this grid size is supported by a grid sensitivity study performed for case A where it was found that the differences of result as compared to a simulation run with a grid width $h = 1/64$ is very small (Ghidersa et al., 2004). At the four side walls of the channel no-slip boundary conditions are imposed. In stream-wise vertical direction the presence and influence of the neighboring unit cells is simulated by periodic boundary conditions. The simulations are started from fluid at rest. The time step width is $\Delta t = 2.5 \times 10^{-5}$. The Courant-Friedrichs-Levy number based on the terminal bubble velocity $U_B \approx 4$ takes a value of $CFL = U_B \Delta t / \Delta x \approx 0.005$.

Table 1
 Geometrical and computational parameters of the simulation runs

Case	L_{fuc}	computational domain	grid	time steps	problem time
A	1	$1 \times 1 \times 1$	$48 \times 48 \times 48$	24,000	0.60
B	1.25	$1 \times 1.25 \times 1$	$48 \times 60 \times 48$	24,000	0.60
C	1.5	$1 \times 1.5 \times 1$	$48 \times 72 \times 48$	26,000	0.65
D	1.75	$1 \times 1.75 \times 1$	$48 \times 84 \times 48$	26,000	0.65
E	2	$1 \times 2 \times 1$	$48 \times 96 \times 48$	28,000	0.70

2.4 Initial bubble shape

We now describe the initial shape of the bubble for the different simulations. In case A it is a sphere with diameter $D_B = 0.858$. For the other cases the initial shape of the bubble is given by an elongated body of revolution, which consists of three parts, see Fig. 1. Let $\eta = r^* / L_{\text{ref}}^*$ be the dimensionless radius of the bubble and $\zeta = \zeta^* / L_{\text{ref}}^*$ the dimensionless distance from the bubble apex. The first two segments of the bubble correspond to the analytical solution for the shape of a semi-infinite Taylor bubble rising in a vertical tube under the assumption of potential flow (Dumitrescu, 1943). The length of the first two segments of the bubble is ζ_{body} . To obtain a closed bubble we approximate its rear by an axisymmetric ellipsoid with aspect ratio $k = a / b > 0$, see Figure 1. Mathematically, the three parts are given by the following functions:

$$\eta = \begin{cases} \eta_1 = [\zeta(0.75 - \zeta)]^{0.5} & \text{for } 0 \leq \zeta \leq \frac{1}{4} \\ \eta_2 = 0.5(1 - 0.25\zeta^{-0.5})^{0.5} & \text{for } \frac{1}{4} < \zeta \leq \zeta_{\text{body}} \\ \eta_3 = \left[b^2 - ((\zeta - \zeta_{\text{body}} - d)/k)^2 \right]^{0.5} & \text{for } \zeta_{\text{body}} < \zeta \leq \zeta_{\text{max}} \end{cases} \quad (7)$$

where b, d and ζ_{max} are given by

$$b = \left[0.25(1 - 0.25\zeta_{\text{body}}^{-0.5}) + \frac{1}{4096} \frac{k^2}{\zeta_{\text{body}}^3} \right]^{0.5}, \quad d = \frac{1}{64} \frac{k^2}{\zeta_{\text{body}}^{1.5}}, \quad \zeta_{\text{max}} = \zeta_{\text{body}} + d + b \cdot k \quad (8)$$

By formulas (7) we ensure that for $\zeta = 0.25$ and $\zeta = \zeta_{\text{body}}$ the curves as well as their first derivatives are continuous. To define the bubble shape we only need to specify ζ_{body} and k . Here, we take the rear of the bubble to be a segment of a sphere, i.e. $k = 1$. The non-dimensional volume of the bubble is given by the integral

$$V_B = \pi \int_0^{0.25} \eta_1^2 d\zeta + \pi \int_{0.25}^{\zeta_{body}} \eta_2^2 d\zeta + \pi \int_{\zeta_{body}}^{\zeta_{max}} \eta_3^2 d\zeta \quad (9)$$

Here, we want to keep the gas hold up constant in all the simulations. Therefore, for each case, we determine ζ_{body} from the condition $V_B = \varepsilon L_{fuc}$.

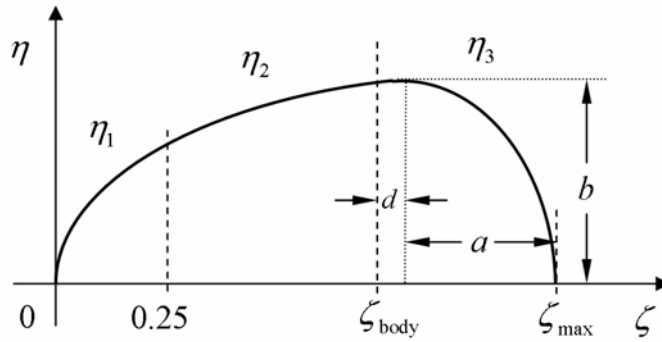


Fig. 1. Sketch of initial bubble shape.

In Figure 2 we show the initial bubble shape for the five cases. Note that in case C the tip of the bubble points downward. By this we intend to investigate if the initial bubble shape has any influence on the steady bubble shape and the terminal bubble velocity.

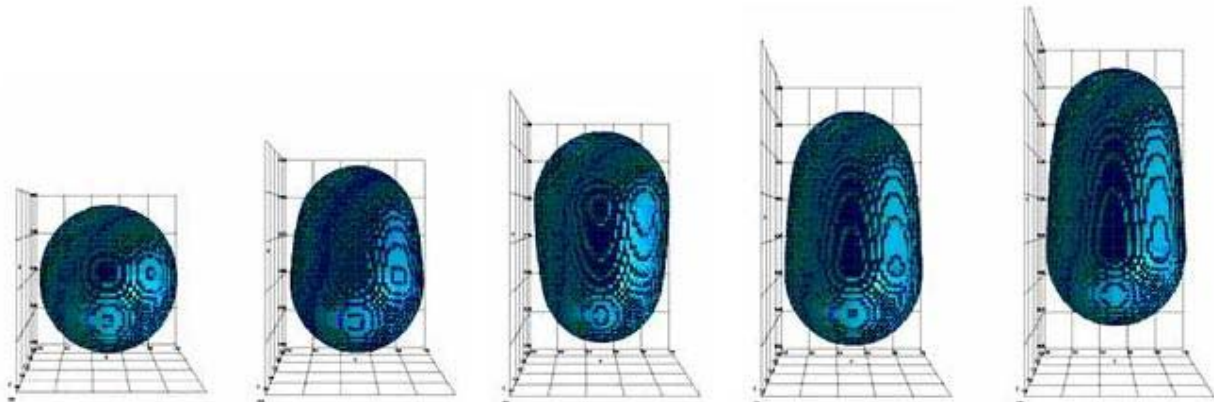


Fig 2. Initial bubble shape for cases A-E (from left to right).

2.5 Physical parameters

In Table 2 we give the physical properties of the fluids. The density and viscosity of the liquid phase are for silicone oil and correspond to the experiments by Thulasidas et al. (1995). While in these experiments the disperse phase is air, in our simulations we increase the gas density by a factor of 10 as compared to air. This is in order to increase the computational efficiency of our explicit time integration scheme, which results in severe time step restrictions if the density ratio is very low (Wörner, 2002). This increase of the gas density is justified due to the results of the numerical study of Wörner (2003). In that paper the influence of the gas-liquid density ratio is investigated for the buoyancy driven rise of an oblate ellipsoidal bubble and a spherical cap bubble. It is found that under proper scaling the steady bubble shape and the velocity field inside the bubble and in the liquid are invariant with respect to a variation of the gas-liquid density ratio. In order to

keep the ratio of the Reynolds numbers in the gas and liquid flow similar to the experiment, we increase the dynamic viscosity of the gas in the computations by a factor of 10, too. Therefore, the gas-liquid kinematic viscosity ratio is the same in the experiment and in our computations. The physical properties given in Table 2 result in a Morton number

$$M \equiv \frac{(\rho_l^* - \rho_g^*) g^* \mu_l^{*4}}{\rho_l^{*2} \sigma^{*3}} = 0.00493 \quad (10)$$

This value is only slightly lower than the one in the experiment, where $M = 0.00498$. In Table 3 we list the reference scales and the non-dimensional groups that appear in the mixture momentum equation. The reference Euler number is estimated from the pressure drop of the single phase flow with the same liquid flow rate as in Thulasidas et al. (1995).

Table 2
 Physical properties of the simulations

ρ_l^*	ρ_g^*	μ_l^*	μ_g^*	σ^*	g^*
957 kg/m ³	11.7 kg/m ³	0.048 Pa s	1.84×10^{-4} Pa s	0.02218 N/m	9.81 m/s ²

Table 3
 Reference scales and dimensionless numbers of the simulations

L_{ref}^*	U_{ref}^*	Re_{ref}	Eo_{ref}	We_{ref}	Eu_{ref}
0.002 m	0.0264 m/s	1.0527	1.065	0.060	27.03

3 Results

3.1 Integral velocities

In Figure 3 we show the time history of the bubble velocity and the mean liquid velocity for the five cases. We see that the mean liquid velocity, U_l , reaches its terminal value after a problem time of only $t \approx 0.1$ which corresponds to about 0.01 seconds. For the bubble itself it takes much more time to reach its terminal velocity. We see that with the increase of the length of the flow unit cell both, the velocity of the bubble and the mean liquid velocity do increase. It may be expected that with further increase of L_{fuc} both U_B and U_l will approach limiting values so that they eventually become independent of L_{fuc} . However, from the results shown in Fig. 3 it appears that this will be the case for values of L_{fuc} much larger than 2.

From Figure 3 we also observe that for case C the time history of U_B in the interval $0.05 < t < 0.3$ qualitatively differs as compared to the other cases. We attribute this to the initial bubble shape of case C which differs from the other cases so far as the bubble tip is oriented downwards, see Fig. 2. However, the terminal values of U_B and U_l do well fall in between those of cases B and D. This indicates that the initial bubble shape has no influence on the final bubble velocity and shape.

In Table 4 we give the computed values for the terminal bubble velocity U_B and the mean liquid velocity U_l . These velocities are displayed in graphical form in Fig. 4 as function of L_{fuc} . Also shown are the gas superficial velocity $J_g = \varepsilon U_B$ and the liquid superficial velocity $J_l = (1 - \varepsilon) U_l$ as well as the total superficial velocity $J_{\text{total}} = J_g + J_l$. The total superficial velocity equals the slug velocity U_{slug} which is the mean axial velocity in any cross section fully occupied by the liquid. From Fig. 4 we see that all the mentioned integral velocities increase with increase of L_{fuc} . However, the differences for cases A and B are very small while they are significant for cases B-E.

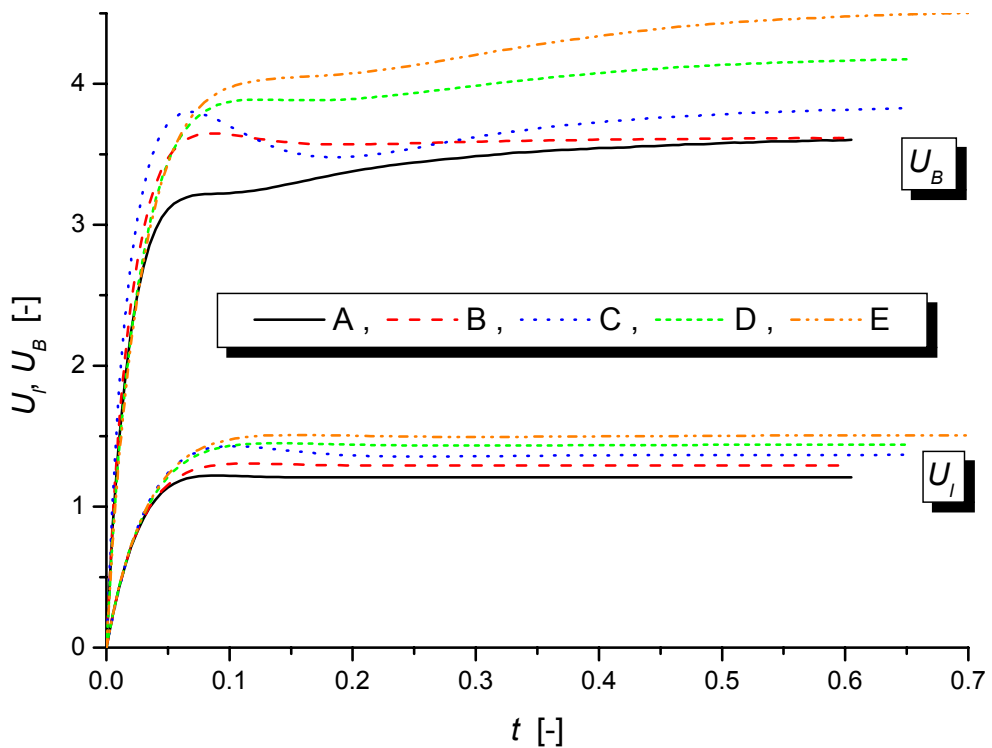


Fig. 3. Time history of bubble velocity, U_B , and mean liquid velocity, U_l .

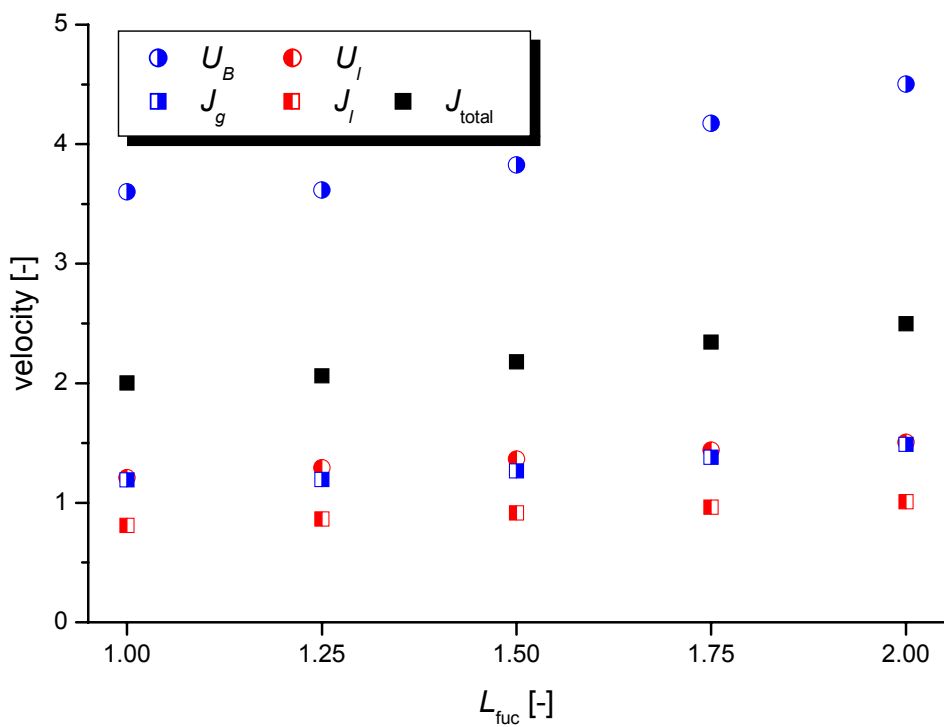


Fig. 4. Terminal integral velocities for different values of the length of the flow unit cell.

Table 4
 Selected simulation results

Case	L_{fuc}	U_B	U_l	D_B	L_B	L_B / L_{fuc}	Ca_B	V	Z
A	1	3.60	1.21	0.81	0.93	0.93	0.204	1.80	0.445
B	1.25	3.61	1.29	0.84	1.05	0.84	0.207	1.75	0.430
C	1.5	3.83	1.37	0.85	1.20	0.80	0.215	1.75	0.430
D	1.75	4.17	1.44	0.85	1.36	0.78	0.238	1.78	0.438
E	2	4.50	1.51	0.85	1.53	0.76	0.253	1.80	0.445

3.2 Bubble shape

Figure 5 shows the left half of the steady bubble shape for all five cases. To allow for a good visualization for each case the results are given for an instant in time when the bubble tip is almost at the top of the computational domain. The visualization of the bubble shape for a certain instant in time is performed as follows. For each mesh cell that contains both phases ($0 < f < 1$) the centroid of the plane representing the interface is computed. The centroids of neighboring mesh cells are then connected to form triangles or quadrangles yielding a closed surface. By this procedure it is possible to determine the bubble dimensions with a resolution that is smaller than the actual mesh width h .

In all five cases the bubble is axisymmetric, i.e. its cross section at any axial position is circular. This is to be expected, since the generally accepted lower limit of the capillary number $Ca_B \equiv \mu_l^* U_B^* / \sigma^*$ for which the bubble shape remains axisymmetric when it moves in a square channel is $Ca_{\text{axi}} = 0.04$ (Ratulowski & Chang, 1989; Thulasidas et al., 1995).

To quantify the bubble shape we give in Table 4 values for the non-dimensional bubble diameter D_B . This is the diameter of the bubble in the cross section where the bubble has its largest lateral extension. We also give values for the non-dimensional bubble length L_B and for the ratio L_B / L_{fuc} . These data are displayed in Fig. 6 for the different values of L_{fuc} . We see that for cases A-C the bubble diameter increases while it is almost constant for cases C, D and E. While the length of the bubble monotonically increases from case A to E, the slope of the ratio L_B / L_{fuc} becomes very small for case C, D, and E. These results suggest that the bubble diameter and the ratio between the bubble length and the length of the flow unit cell may become independent of L_{fuc} for $L_{\text{fuc}} > 2$.

A detailed comparison of the bubble shape shows that the radius of curvature of the bubble tip, r_{tip} , is almost the same for case A and B. Also for case C, D and E the value of r_{tip} is about the same, but is somewhat smaller than for case A and B. However, for all cases A-E the value of r_{tip} is clearly smaller than that of the analytical solution obtained by potential flow theory for a bubble rising in a pipe, see Section 2.4. The radius of curvature at the bubbles rear is a little bit smaller for case A than for case B, both being smaller than those of case C, D and E which is almost the same for these three cases.

Figure 5 also shows the velocity field in the axial mid-plane for the five cases. In the left half of the figure the velocity field is shown for a fixed frame of reference while in the right half it is displayed for the frame of reference moving with the bubble, i.e. the bubble velocity is subtracted from the vertical velocity component. We begin our discussion with the velocity field in the fixed frame of reference. The velocity profile in the liquid slug has the form of a parabola and is similar for all five cases. In the region where the liquid film is very thin the liquid velocity is almost zero. In the frame of reference moving with the bubble the flow inside the bubble can be analyzed. We find that there is one big vortex which occupies almost the complete bubble. In the rear part of the bubble, however, in this frame of reference the velocity is almost zero. As regards to the flow in the liquid, the velocity profiles in the frame of reference moving with the bubble indicate the part of the liquid slug that is moving with the velocity of the bubble.

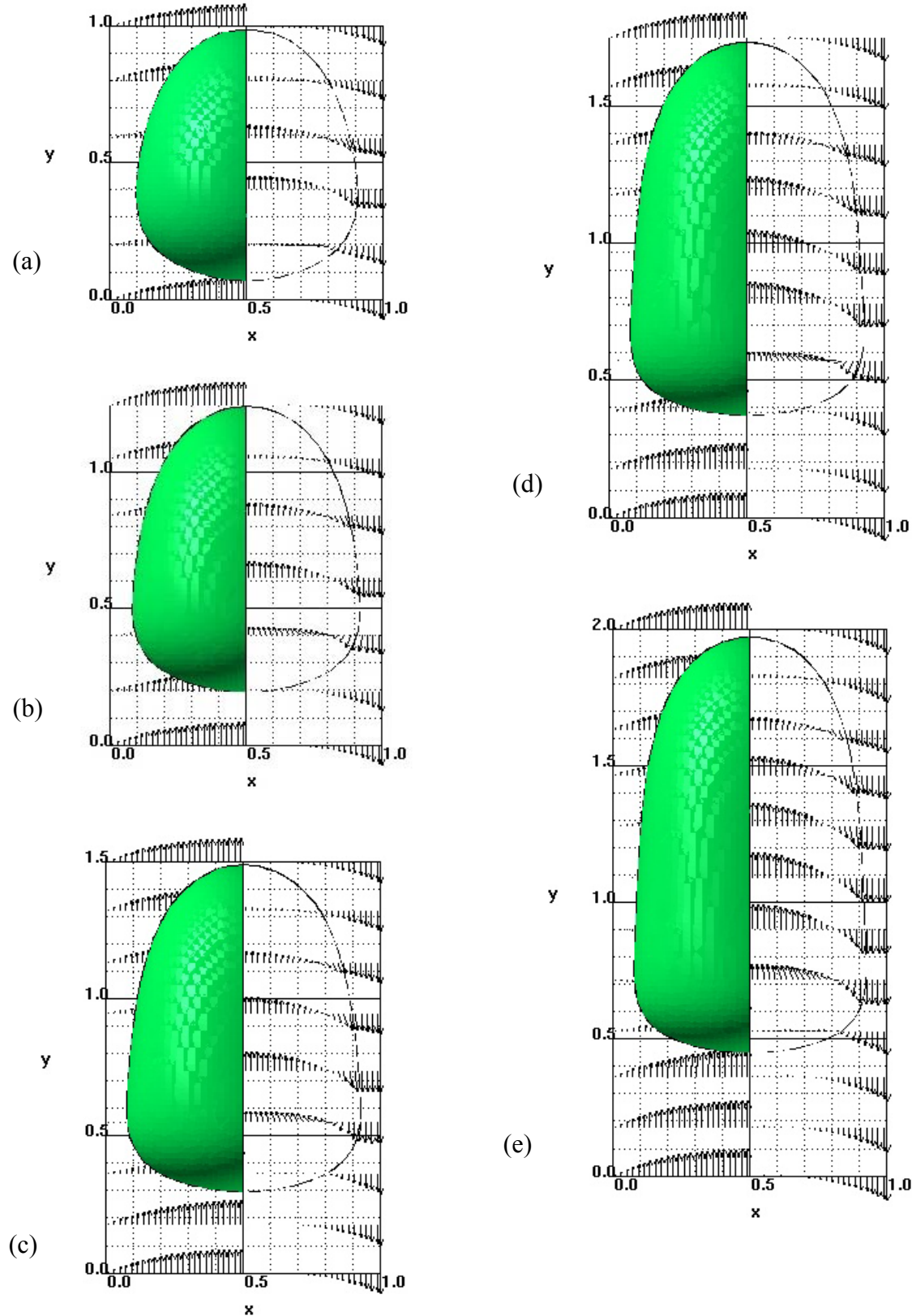


Fig. 5. Bubble shape and velocity field in plane $z = 0.5$ for fixed frame of reference (left half) and for frame of reference linked to the bubble (right half) for (a): case A, $t = 0.595$, (b): case B, $t = 0.38$, (c): case C, $t = 0.44$, (d): case D, $t = 0.51$, (e): case E, $t = 0.54$. In y-direction only every 8th vector is displayed.

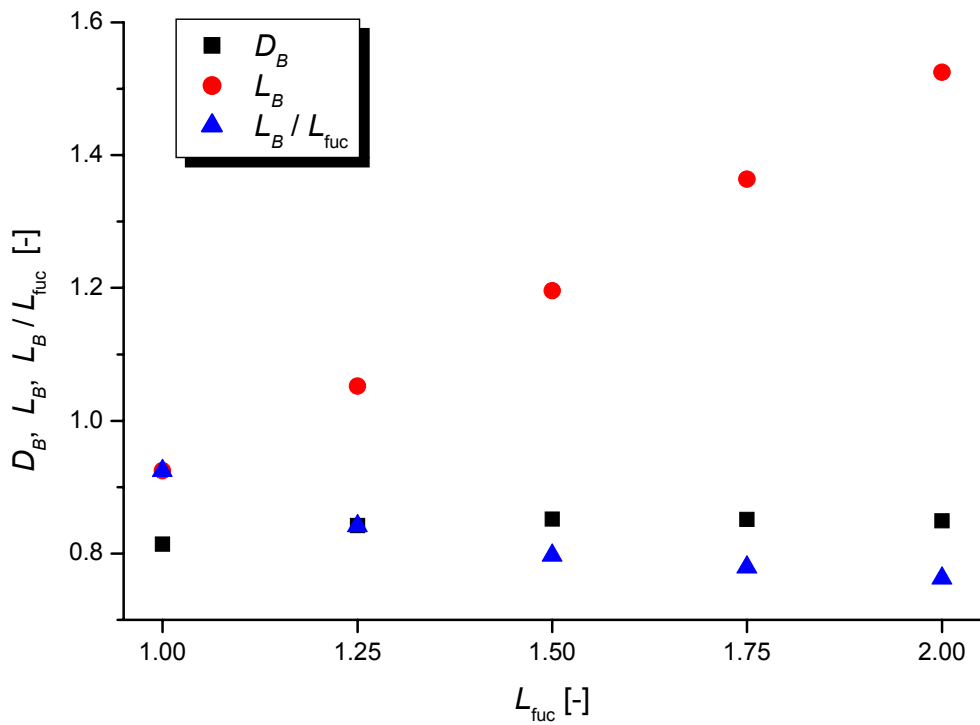


Fig. 6. Bubble diameter and bubble length for different values of the length of the flow unit cell.

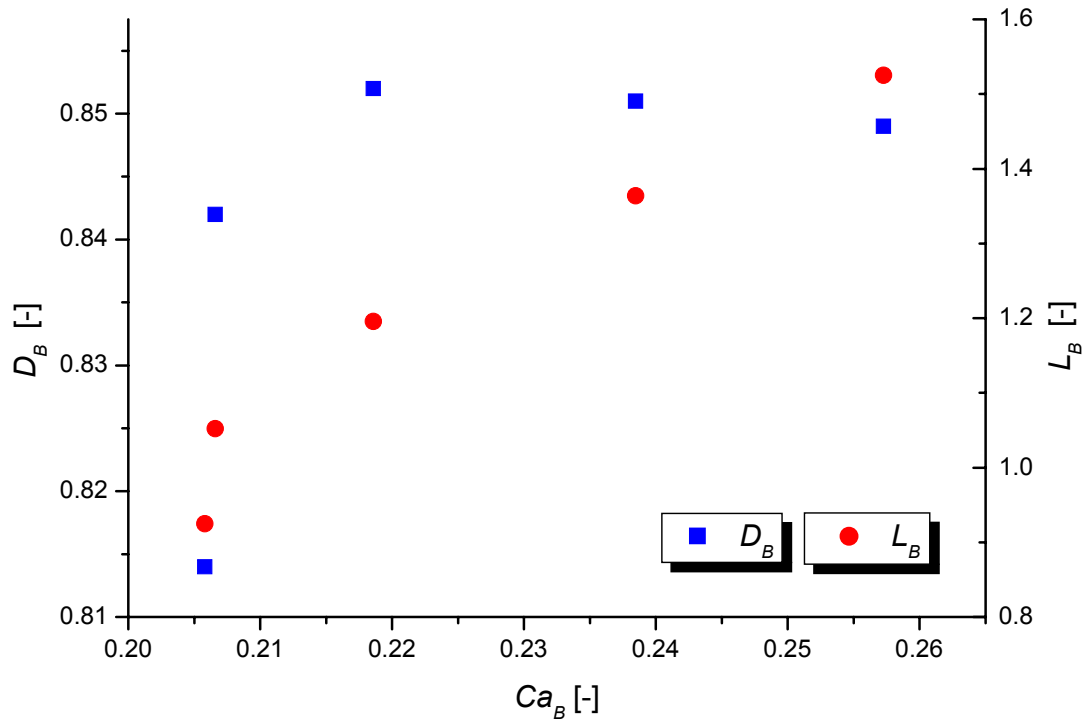


Fig. 7. Bubble diameter and bubble length as function of the capillary number.

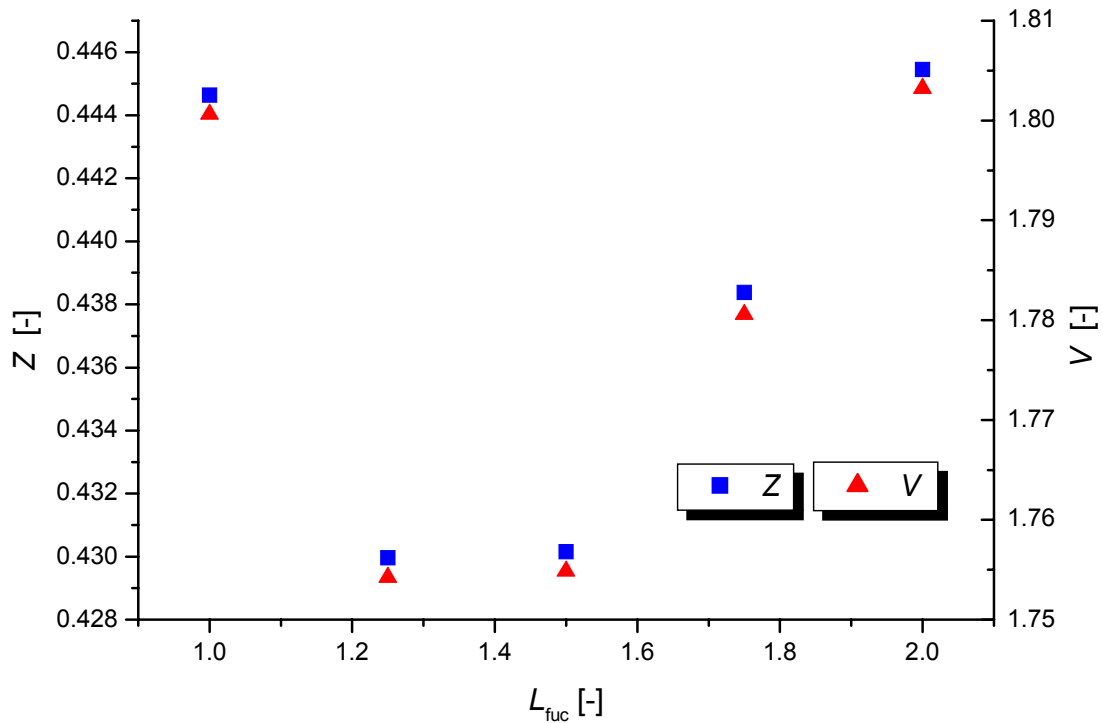


Fig. 8. Non-dimensional velocities V and Z for different values of the length of the flow unit cell.

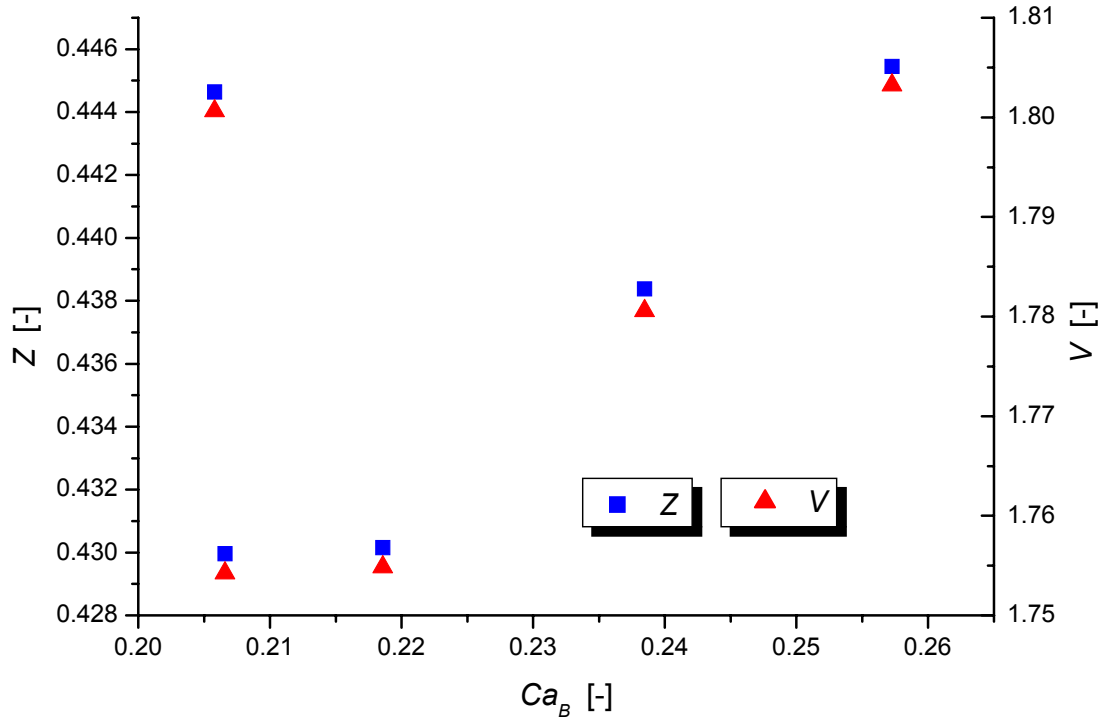


Fig. 9. Non-dimensional velocities V and Z as function of the capillary number.

3.3 Verification and capillary number dependence

The dominant forces for two phase flow in small channels are the viscous force and the surface tension force. The ratio between these two forces constitutes the capillary number. Quantities of interest such as the bubble diameter D_B^* or the liquid film thickness $d_l^* = (W^* - D_B^*) / 2$ are therefore usually correlated in terms of $Ca_B \equiv \mu_l^* U_B^* / \sigma^*$. Since μ_l^* and σ^* are constant Ca_B can be interpreted as non-dimensional bubble velocity. The values of Ca_B for the five cases are listed in Table 4. Because the bubble velocity increases with L_{fuc} the same holds for Ca_B .

Thulasidas et al. (1995) give experimental result for the bubble diameter, for the ratio of bubble velocity to total superficial velocity, $Z = U_B^* / J_{\text{total}}^*$, and for the relative bubble velocity $V = (U_B^* - U_{\text{slug}}^*) / U_B^*$ in terms of Ca_B . In our simulations the range of the capillary number is $0.204 \leq Ca_B \leq 0.253$. For this range Thulasidas et al. (1995) give for the different quantities values falling (with some scattering) in the range $0.82 < D_B < 0.86$, $0.435 < Z < 0.475$ and $1.68 < V < 1.84$, respectively. Thus, our computational results for D_B , Z and V listed in Table 4 do well agree with these experimental data.

In Figure 7 we show the computed values of D_B over Ca_B . We see that first there is an increase of D_B with Ca_B (case A, B, C) but then there is a decrease (case C, D and E). This result is in contrast to the experimental study of Thulasidas et al. (1995) who find a monotonic decrease of the bubble diameter with increasing capillary number. We interpret this finding as follows. In the experiments of Thulasidas et al. (1995) the bubble length is always larger than the width of the channel. In our simulations this is, however, not the case and the ratio $L_B = L_B^* / W^*$ ranges from 0.93 in case A to 1.53 for case E. In Figure 7 we also show the variation of L_B with Ca_B . The data suggest that there may exist a critical bubble length $L_{B,\text{crit}} \approx 1.2$. For values smaller than $L_{B,\text{crit}}$ the bubble diameter increases with increasing capillary number while for values larger than $L_{B,\text{crit}}$ it decreases. However, the accurate determination of $L_{B,\text{crit}}$ requires further simulations especially in the range $1.25 < L_{fuc} < 1.75$. While the computational results for D_B over Ca_B in Fig. 7 show a local maximum, we find for the dependence of V and Z on L_{fuc} and Ca_B a local minimum, see Figs. 8 and 9. These results suggest that there is a significant change in the flow conditions when the bubble length exceeds $L_{B,\text{crit}}$.

4 Conclusions

In this paper we investigate bubble train flow in a square vertical mini-channel of 2 mm width by direct numerical simulations based on the volume of fluid technique for interface tracking. We are especially interested in the influence of the length of the flow unit cell. Five simulations are performed where the ratio between flow unit cell length and channel width takes values of $L_{fuc} = 1, 1.25, 1.5, 1.75$ and 2. All the other physical and numerical parameters are kept constant. The computations are verified by experimental data (Thulasidas et al., 1995) where air is the disperse phase and silicon oil is the continuous phase. The computational results for the diameter of the bubble and for characteristic velocities are in agreement with respective experimental data.

The computational results show that the bubble velocity and the mean liquid velocity increase with increasing length of the flow unit cell. The increase of the bubble velocity results in an increase of the capillary number. The diameter of the axisymmetric bubble first increases with L_{fuc} but is almost constant for $L_{fuc} > 1.5$. Also the radius of curvature of the bubble tip and bubble rear become independent of L_{fuc} for $L_{fuc} > 1.5$. The radius of curvature is, however, smaller than that corresponding to the analytical potential flow solution for a Taylor bubble rising in a pipe through otherwise stagnant liquid. An analysis of the local velocity field shows that in the liquid film the velocity is almost zero, while the flow in the bubble is dominated by one large vortex.

Correlating the dimensionless bubble diameter D_B and the relative bubble velocity Z with the capillary number Ca_B gives the interesting and new result that these relations are not monotonic as experimental data from literature suggest. Instead, there exists a maximum for $D_B(Ca_B)$ and a

minimum for $Z(Ca_B)$. Our results indicate that this maximum respectively minimum may be determined by a ratio of bubble length to channel width of about 1.2. To clarify this topic, however, further simulations with values of the length of the flow unit cell in the range $1.25 < L_{fuc} < 1.75$ are required and will be performed in future. We remark that an experimental investigation of this aspect may be difficult for two reasons. First, the length of the flow unit cell is not a parameter which can be easily adjusted. Second, when the length of the liquid slug becomes small the bubble train flow may become unstable and coalescence of neighboring bubbles may occur.

Acknowledgement

The authors thank D.A. Herban for developing the program for initialization of the Taylor bubble.

References

- Dumitrescu, D.T., 1943. Strömung an einer Luftblase im senkrechten Rohr. ZAMM 23, 139–149.
- Ghidersa, B.E., Wörner, M., Cacuci, D.G., 2004. Exploring the flow of immiscible fluids in a square vertical mini-channel by direct numerical simulation. To be published in Chem. Eng. J.
- Ghidersa, B.E., 2003. Finite-volume-based volume-of-fluid method for the simulation of two-phase flow in small rectangular channels. Ph.D. thesis, University Karlsruhe.
(<http://www.ubka.uni-karlsruhe.de/cgi-bin/psview?document=2003/maschinenbau/10>)
- Ghidersa, B.E., Wörner, M., Cacuci, D.G., 2003. Numerical simulation of bubble-train flow in a small channel of square cross-section. Proc. German-Japanese Workshop on Multi-phase Flow, Karlsruhe, Germany, August 25-27, 2002, Forschungszentrum Karlsruhe FZKA 6759, March 2003, G1–G9. (<http://bibliothek.fzk.de/zb/berichte/FZKA6759.pdf>)
- Hessel, V., Hardt S., Löwe, H., 2004. Chemical micro process engineering. Wiley, Weinheim.
- Meinhart, C.D., Wereley, S.T., Santiago, J.G., 1999. PIV measurement of a microchannel flow. Exp. Fluids 27, 414–419.
- Ratulowski, J., Chang, H.-C., 1989. Transport of gas bubbles in capillaries. Phys. Fluids A1, 1642–1655.
- Sabisch, W., Wörner, M., Grötzbach, G., Cacuci, D.G., 2001. 3D volume-of-fluid simulation of a wobbling bubble in a gas-liquid system of low Morton number. Proc. 4th Int. Conf. Multiphase Flow, May 27 – June 1, 2001, New Orleans, Louisiana, USA, CD-ROM.
- Schubert, K., Brandner, J., Fichtner, M., Linder, G., Schygulla, U., Wenka, A., 2001. Microstructure devices for applications in thermal and chemical engineering. Microscale Thermophysical Engineering 5, 17–39.
- Thulasidas, T.C., Abraham M.A., Cerro, R.L., 1995. Bubble train flow in capillaries of circular and square cross section. Chem. Eng. Science 50, 183–199.
- Wörner, M., Sabisch, W., Grötzbach, G., Cacuci, D.G., 2001. Volume-averaged conservation equations for volume-of-fluid interface tracking. Proc. 4th Int. Conf. Multiphase Flow, May 27 – June 1, 2001, New Orleans, Louisiana, USA, CD-ROM.
- Wörner, M., 2002. The influence of the gas-liquid density ratio on shape and rise velocity of an ellipsoidal bubble: a numerical study by 3D volume-of-fluid computations. Proc. 1st Int. Berlin Workshop on Transport Phenomena with Moving Boundaries, October 11–12, 2001, Berlin, Germany, F.-P. Schindler (Ed.), Fortschritt-Berichte VDI Reihe 3 Verfahrenstechnik Nr. 738, 67–84, VDI Verlag Düsseldorf.
- Wörner, M., 2003. Invariance of the velocity field induced by a bubble rising steadily through liquid under variation of the gas-liquid density ratio. In: T. Schulenberg, M. Ozawa, G. Grötzbach (Eds.), Proc. German-Japanese Workshop on Multiphase Flow, Karlsruhe, Germany, August 25–27, 2002, Forschungszentrum Karlsruhe, FZKA 6759, March 2003, G10–G21. (<http://bibliothek.fzk.de/zb/berichte/FZKA6759.pdf>)